





Fast, noise-free atomic optical memory with 35-percent end-to-end efficiency

Omri Davidson ¹, Ohad Yogev¹, Eilon Poem ¹ & Ofer Firstenberg ¹

Coherent optical memories will likely play an important role in future quantum communication networks. Among the different platforms, memories based on ladder-type orbital transitions in atomic gasses offer high bandwidth (>100 MHz), continuous (on-demand) readout, and low-noise operation. Here we report on an upgraded setup of our previously-reported fast ladder memory, with improved efficiency and lifetime, and reduced noise. The upgrade employs a stronger control field, wider signal beam, reduced atomic density, higher optical depth, annular optical-pumping beam, and weak dressing of an auxiliary orbital to counteract residual Doppler-broadening. For a 2 ns-long pulse, we demonstrate 53% internal efficiency, 35% end-to-end efficiency, 3×10^{-5} noise photons per pulse, and a $1/e$ lifetime of 108 ns. This combination of performances is a record for continuous-readout memories.

¹Department of Physics of Complex Systems, Weizmann Institute of Science, Rehovot 7610001, Israel. email: omri.davidson@weizmann.ac.il

The generation of multi-photon states is highly desirable for quantum information processing applications such as photonic quantum computation and communication¹. Quantum optical memories are likely to be critical components in such applications due to the probabilistic nature of photon sources and photonic gates². Memories for classical and quantum light have been demonstrated in a plethora of systems, including cold atoms^{3–5}, hot atomic vapor^{6–8}, solid-state artificial atoms^{9–11}, and all-optical storage loops^{12–14}. With the exception of storage loops, these memories can offer continuous (on-demand) readout, required for synchronizing continuously pumped photon sources^{15–17}.

Memories based on the spin coherence of atomic ensembles, where both the signal photon and classical control field couple to the ground electronic orbital, have been extensively studied due to their potential for high storage efficiency^{18–21} and long storage time^{22–25}. However, it is difficult to obtain noise-free operation in these memories due to four-wave mixing (FWM) noise²⁶ and, in memories based on warm atomic ensembles, spontaneous Raman scattering from imperfect optical pumping²¹. These issues become even more pronounced, and eventually detrimental, when operating at warm temperatures and at high bandwidths that are comparable to the hyperfine splitting. Additionally, low-noise operation requires filtering out the strong control field, which typically requires etalon filters that reduce the signal transmission and hence the memory's end-to-end efficiency^{18–21}.

An alternative to the spin memory is the orbital memory^{27–29}, where the excitation scheme is of a ladder-type, and the light is stored on a doubly-excited orbital. Although the memory lifetime is inherently limited by the lifetime of the orbital level, orbital memories are immune to FWM noise due to the ladder excitation scheme and the wavelength mismatch between the signal and control transitions^{27,28}. Since the storage level is not populated even at high temperatures, the spontaneous Raman scattering noise is eliminated. Furthermore, the wavelength mismatch also enables the filtering of the strong control field from the retrieved signal field using conventional thin-film interference filters (IFs) with high transmission.

A fast ladder memory (FLAME) based on off-resonant cascaded absorption was demonstrated in cesium vapor by Kaczmarek et al.²⁸ and rubidium vapor by Thomas et al.²⁹. In these demonstrations,

the large wavelength mismatch between the signal and control fields resulted in a substantial residual Doppler broadening that limits the memory lifetime to a few ns. A much smaller mismatch exists for the ladder scheme $|5S_{1/2}\rangle \rightarrow |5P_{3/2}\rangle \rightarrow |5D_{5/2}\rangle$ in rubidium, for which the signal and control wavelengths are 780 and 776 nm, respectively. As demonstrated by Finkelstein et al.²⁷, the reduced residual Doppler broadening of this cascaded transition enables a memory lifetime of ~ 130 ns in the absence of other decoherence mechanisms.

Here we report on an upgraded FLAME setup (FLAME-2) which has several improvements over the original demonstration (FLAME-1)²⁷. FLAME-2 uses an auxiliary, off-resonant dressing field that counteracts the residual Doppler broadening and further increases the memory lifetime³⁰. To increase the memory efficiency and reduce the noise, FLAME-2 employs a longer vapor cell, which provides higher optical depth (OD) at a lower atomic density, and an annular optical pumping beam. Finally, the control field of FLAME-2 is stronger, which increases the memory efficiency for the on-resonance storage scheme, and the signal beam diameter is larger, reducing time-of-flight decoherence. As part of the characterization of FLAME-2, we study on-resonance storage (also known as electromagnetically-induced-transparency storage³¹) and off-resonance storage (pertaining to Raman storage³²) of nanosecond-long pulses with variable width.

Results

Experimental scheme. We use the stretched states of the ^{87}Rb level system shown in Fig. 1a. The signal pulse with a wavelength of 780 nm couples the $|5S_{1/2}, F=2, m_F=2\rangle \rightarrow |5P_{3/2}, F=3, m_F=3\rangle$ transition with a detuning $\Delta=0$ ($\Delta=1.1$ GHz) for on-resonance (off-resonance) storage. The control field with a wavelength of 776 nm is detuned from the $|5P_{3/2}, F=3, m_F=3\rangle \rightarrow |5D_{5/2}, F=4, m_F=4\rangle$ transition such that the two-photon transition $|5S_{1/2}\rangle \rightarrow |5P_{3/2}\rangle \rightarrow |5D_{5/2}\rangle$ is almost on-resonance. The auxiliary dressing field with a wavelength of 1274 nm is detuned by $\Delta_d = -570$ MHz from the $|5D_{5/2}\rangle \rightarrow |28F_{7/2}\rangle$ transition. Lastly, the pump and repump fields, used to optically pump the atoms to the maximal spin state $|5S_{1/2}, F=2, m_F=2\rangle$, have a wavelength of 795 nm and couple the $|5S_{1/2}, F=2\rangle \rightarrow$

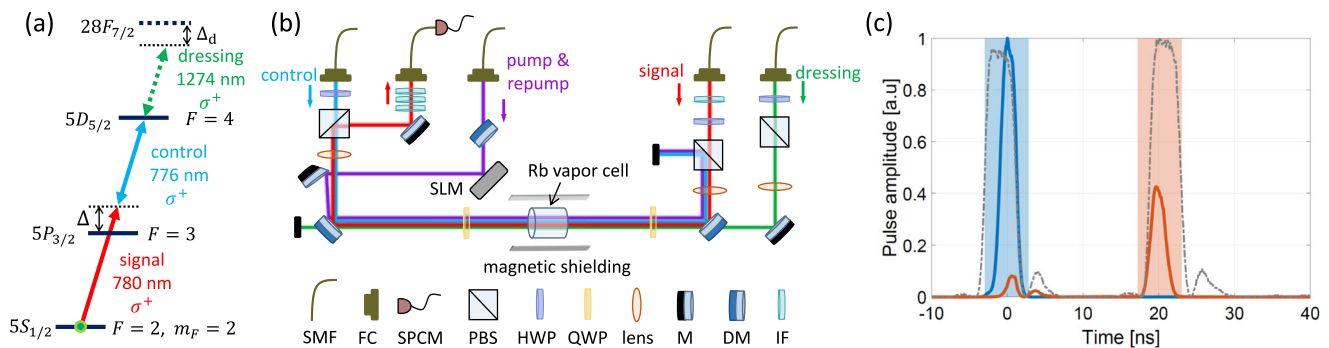


Fig. 1 FLAME-2 system. **a** The ladder-level scheme of ^{87}Rb . Initially, the atoms are optically pumped to the $|5S_{1/2}, F=2, m_F=2\rangle$ ground state, where F is the total angular momentum of the valence electron and m_F is the angular momentum projection on the optical axis. The memory operates with all-orbital transitions to generate coherence between the ground state and the doubly-excited state $|5D_{5/2}, F=4, m_F=4\rangle$. The latter is off-resonantly coupled to the auxiliary state $|28F_{7/2}\rangle$ in order to compensate for the residual Doppler broadening of the $|5S_{1/2}\rangle \rightarrow |5P_{3/2}\rangle \rightarrow |5D_{5/2}\rangle$ transition. **b** The experimental setup. The signal and control beams counter-propagate inside the vapor cell. The pump and repump beams are reflected from a spatial light modulator (SLM) to generate an annular beam inside the vapor cell and are inserted with a slight angle to the optical axis. The dressing beam is combined with the signal beam on a dichroic mirror. **c** Characteristic measurement with and without the memory operation. Shown are the reference signal pulse (blue), the stored and retrieved pulse for on-resonance storage (orange), and the control pulses (dashed-dotted gray). The shaded areas indicate the integration window size used for calculating memory efficiency. DM dichroic mirror, FC fiber coupler, FLAME fast ladder memory, HWP half-wave plate, IF interference filter, M mirror, PBS polarizing beam splitter, QWP quarter-wave plate, SMF polarization-maintaining single-mode fiber, SPCM single-photon counting module.

$|5P_{1/2}, F = 2\rangle$ and $|5S_{1/2}, F = 1\rangle \rightarrow |5P_{1/2}, F = 2\rangle$ transitions, respectively (not shown in Fig. 1a). Experimental details on the generation of the light fields used in the experiment are given in the methods section.

Figure 1b shows the experimental setup. All fields are σ^+ polarized inside the medium. The signal field counter-propagates with the control field inside a 25-mm-long isotopically purified ^{87}Rb vapor cell. The cell is placed inside three layers of mu-metal magnetic shielding and heated to $\sim 65^\circ\text{C}$. The dressing field co-propagates with the signal field.

The counter-propagating signal and control fields render the residual Doppler broadening of the two-photon transition very small. Nevertheless, to further suppress the residual Doppler broadening caused by their small wavelength difference, we employ a “continuous protection” scheme previously developed in our lab³⁰. Here, the velocity-dependent Doppler shift is continuously compensated by a velocity-dependent light shift, induced by the auxiliary dressing field (see Methods).

The pump and repump fields are reflected from a spatial light modulator (SLM) to generate an annular beam that does not overlap the signal inside the vapor cell. During the pumping, part of the atomic population is excited to the $5P_{1/2}$ level. These atoms can collide and transfer the population to the $5D_{5/2}$ level via an energy-pulling process³³. This incoherent population can then decay to the $5P_{3/2}$ state, from which it fluoresces and adds noise to the signal channel²⁷. The annular beam spatially separates the pump beams from the signal, and thus reduces the noise in the output mode. The optical pumping efficiency of the $F = 2$ ground level to the maximal spin state ($m_F = 2$) is $94 \pm 2\%$. Errors of system characterization represent 1 standard deviation (s.d.) of measurement uncertainty.

The output signal is sent to a single-photon counting module through a single-mode, polarization-maintaining fiber. There is no need to use etalon filters to clean the signal, due to the wavelength difference between the signal and control fields. Instead, we use two narrow-band IFs with 3-nm full-width at half-maximum (FWHM) in the output signal channel to filter out the residual control, pump, and repump fields, and a short-pass IF to filter out the residual dressing field. Additionally, we have one IF in the input signal channel, which prevents residual control light from coupling into the signal input fiber; This light might undergo spontaneous Raman scattering inside the fiber³⁴, which is frequency shifted and, therefore, partially transmitted through the IF of the output signal. Lastly, we use a dichroic mirror in the pump-repump input channel to block residual 780-nm light. The transmission of the signal field through the memory setup, from immediately after the input signal beam fiber and into and out of the output fiber, is $66 \pm 2\%$. It is comprised of transmission through the vapor cell ($88 \pm 1\%$), transmission through the optical filters ($94 \pm 1\%$), coupling to the output fiber ($88 \pm 2\%$), and the transmission of all other optical elements ($91 \pm 2\%$). In the off-resonance storage, the transmission through the vapor cell is reduced to $75 \pm 2\%$ due to absorption by residual ^{85}Rb .

Figure 1c shows a typical measurement of the memory experiment. Initially, we measure the signal pulse (count histogram shown in blue) when it is far-detuned from the atomic absorption line. Next, we turn on the control pulses (dashed-dotted gray) and again measure the signal output (orange; here, shown for on-resonance storage). The first control pulse generates a coherent absorption of the signal field and maps it into the coherence between the ground and doubly-excited state, which is retrieved with the application of the second control pulse. Throughout the paper, unless specified otherwise, the signal pulse is a Gaussian pulse with an FWHM of 2 ns. The shaded areas in Fig. 1c (light blue and light orange) are the

integration windows (6-ns long) used to calculate the total photon number in the reference and retrieved pulses from which we calculate the memory efficiency. For the noise measurements, we block the signal input and integrate the photon counts in the same time window as for the retrieved pulse.

Memory characterization. We begin the memory characterization by optimizing the length of the control pulse, the two-photon detuning, and the OD to achieve maximal storage and retrieval efficiency. We find the optimal control FWHM to be 4 ns (3 ns) for on-resonance (off-resonance) storage. We note that further increasing the control pulse length reduces the memory efficiency, which might not be expected for on-resonance storage. We attribute this to a reduction in the control pulse amplitude for longer pulses in our system. The optimal two-photon detuning is found at slightly negative values of -50 MHz (-20 MHz), providing a relative efficiency increase of $2 \pm 1\%$ ($1 \pm 1\%$) for on-resonance (off-resonance) storage. In the off-resonance storage, this nonzero optimal detuning is due to control-induced light-shifts. In the on-resonance storage, it is due to the residual absorption of un-pumped atoms to the Doppler-broadened $|5P_{3/2}, F = 1, 2\rangle$ states. We set the vapor temperature such that the OD, measured on the $|5S_{1/2}, F = 2\rangle \rightarrow |5P_{3/2}, F = 3\rangle$ transition, is $\text{OD} = 19 \pm 1$. Further increasing the OD saturates the storage efficiency while increasing the noise induced by the optical pumping beams.

Figure 2 shows the memory efficiency versus storage time t with and without the dressing field for on-resonance and

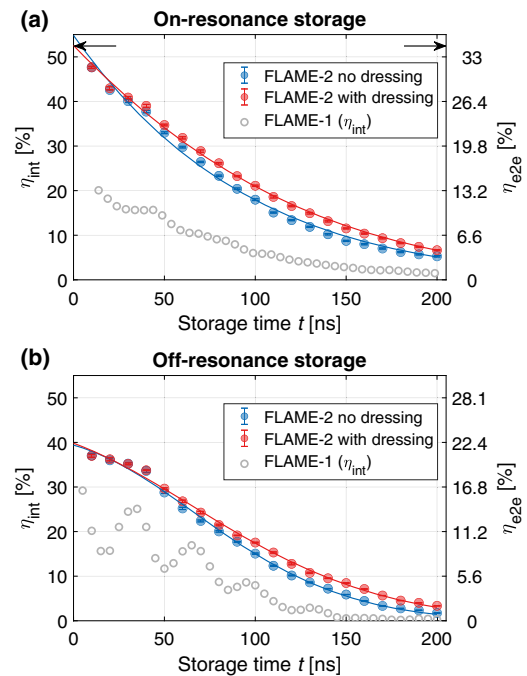


Fig. 2 Memory efficiency. **a, b** Efficiency (storage and retrieval) versus the storage time for **(a)** on-resonance and **(b)** off-resonance storage, without the dressing field (blue) and with the dressing field (red). The left axis is the internal memory efficiency (η_{int}), and the right axis is the memory end-to-end efficiency (η_{e2e}) that includes the signal transmission through the entire memory setup. Circles are the measured data; the standard deviation of the mean of repeated measurements is smaller than the circles' size. The lines are fits to a model comprising exponential and Gaussian decays. The black arrows in **(a)** show the zero-time efficiency. For comparison, we show in gray the internal efficiency of FLAME-1²⁷ (see Memory characterization section for details).

off-resonance storage. We find that the memory efficiency is higher for on-resonance storage when there is sufficient control power. This is to be expected, primarily as our control pulses are not chirped, as required for optimal off-resonance storage³⁵.

Adding the dressing field imparts a velocity-dependent light shift which counteracts the motional decoherence due to the residual Doppler broadening of the $|5S_{1/2}\rangle \rightarrow |5P_{3/2}\rangle \rightarrow |5D_{5/2}\rangle$ transition³⁰. The dressing is kept constantly on, and we observe almost no decrease in memory short-time efficiency. The benefit of the dressing field is most significant at long storage times ($t > 80$ ns), where it increases the memory efficiency by $>10\%$.

We model the memory efficiency versus time as $\eta(t) = \eta(0)e^{-t^2/2\tau_\sigma^2 - t/\tau_\gamma}$, with Gaussian (τ_σ) and exponential (τ_γ) decoherence times. The Gaussian term originates from the residual Doppler broadening and the Maxwell-Boltzmann velocity distribution, whereas the exponential term originates mainly from the finite lifetime of the $5D_{5/2}$ level and the time-of-flight broadening through the beam³⁶. We extract the memory $1/e$ lifetime τ_s from $\eta(\tau_s) = \eta(0)e^{-1}$ (see Finkelstein et al.²⁷ for details). Using the dressing field increases the $1/e$ lifetime from $\tau_s = 90 \pm 3$ ns (102 ± 2 ns) to $\tau_s = 108 \pm 2$ ns (113 ± 2 ns) for on-resonance (off-resonance) storage, while keeping the zero-time efficiency $\eta(0)$ almost unchanged. With the dressing field, we measure an internal (end-to-end) short-time memory efficiency of $\eta_{\text{int}}(0) = 52.6 \pm 0.8\%$ [$\eta_{\text{e2e}}(0) = 34.7 \pm 1.2\%$] for the on-resonance storage, and $\eta_{\text{int}}(0) = 39.8 \pm 0.6\%$ [$\eta_{\text{e2e}}(0) = 22.3 \pm 0.9\%$] for the off-resonance storage. Here the errors are 1 s.d. of the fit uncertainty.

For the sake of comparison, Fig. 2 also shows $\eta_{\text{int}}(t)$ of the original FLAME-1. The most significant increase in memory efficiency is observed for on-resonance storage. The temporal oscillations, which arise in FLAME-1 from destructive interference between $5D_{5/2}$ hyperfine states due to imperfect optical pumping²⁷, are nearly eliminated in FLAME-2. Note that $\eta_{\text{e2e}}(t)$ of FLAME-1 is higher than shown in Fig. 2 by 18% (39%) for on-(off-) resonance storage, mainly due to better transmission of the glass cell windows (and, in the off-resonance case, lower residual ^{85}Rb absorption due to different signal detuning). The end-to-end efficiency of FLAME-2 and FLAME-1 is compared in Table 1.

The dependence of the memory efficiency on the peak power of the control field is shown in Fig. 3a for a storage time of 20 ns. For each control power, we optimize the control pulse timing and find that higher control powers require earlier timing to maximize the efficiency. On-resonance storage reaches higher efficiencies but necessitates a stronger control field, as it requires generating a deep-enough transparency window within the Doppler-broadened absorption line.

Figure 3b shows the mean number of added noise photons from memory versus the control power. The noise per pulse caused by the pump beams is $\nu_p = (0.92 \pm 0.07) \times 10^{-5}$ photons. The noise originating from the control field increases linearly to a level of $\nu_c(P_c = 1 \text{ W}) = (1.67 \pm 0.16) \times 10^{-5}$ photons for on-resonance storage and $\nu_c(P_c = 1 \text{ W}) = (1.46 \pm 0.14) \times 10^{-5}$ photons for off-resonance storage, where P_c is the control power. This residual noise originates from reflection and perhaps a

nonlinear frequency shift of the control field at the vapor cell facets. The dressing field does not add noise within the measurement uncertainty.

We study the memory bandwidth in Fig. 4. Here, for each signal pulse length, the control power and timing are optimized. For all measured signal pulses, the on-resonance storage has a higher efficiency than the off-resonance storage. As expected, the highest efficiency is obtained for the longer (>1.5 ns) signal pulses. While the efficiency reduces for shorter pulses, the effective fractional delay, which determines the potential enhancement of multiphoton rates in a synchronization application², is actually increased when shortening the signal photons.

Discussion

Table 1 compares the performance of the upgraded memory FLAME-2 to the original FLAME-1²⁷. In FLAME-1, the off-resonance storage was slightly more efficient than the on-resonance storage, whereas in FLAME-2, the on-resonance storage is more efficient. This expected result is mainly due to

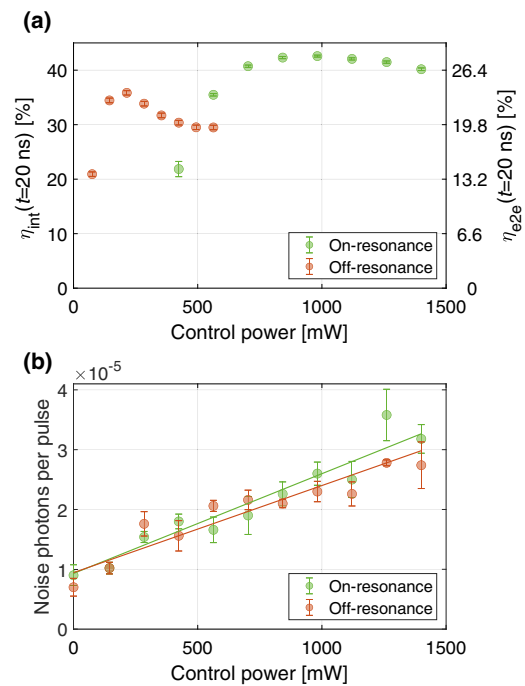


Fig. 3 Dependence of efficiency and noise on the control power. **a** The memory efficiency at a storage time of 20 ns. Note that here and in Fig. 4, the η_{e2e} axis refers to the end-to-end efficiency of the on-resonance storage; the off-resonance storage efficiency is 15% lower due to absorption by residual ^{85}Rb atoms. **b** The mean number of noise photons per retrieved pulse. The lines are a linear fit. Results are shown for (green) on-resonance storage and (orange) off-resonance, both with the dressing field. In **(a, b)** the error bars are the standard deviation of the mean of repeated measurements.

Table 1 Comparison of this work (FLAME-2) and the original demonstration (FLAME-1)²⁷.

	Internal efficiency $\eta_{\text{int}}(0)$ [%]	End-to-end efficiency $\eta_{\text{e2e}}(0)$ [%]	$1/e$ lifetime τ_s [ns]	Noise photons ν [10^{-5}]
FLAME-2 On-resonance	52.6 ± 0.8	34.7 ± 1.2	108 ± 2	2.6 ± 0.2
FLAME-1 On-resonance	22.0 ± 0.4	17.1 ± 0.3	82 ± 1	19 ± 1
FLAME-2 Off-resonance	39.8 ± 0.6	22.3 ± 0.9	113 ± 2	1.2 ± 0.2
FLAME-1 Off-resonance	32 ± 1	25.1 ± 0.8	86 ± 2	5.8 ± 0.4

We quote the performance of on-resonance storage and off-resonance storage in both experiments. FLAME fast ladder memory.

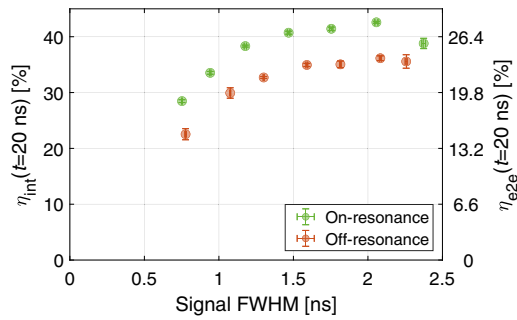


Fig. 4 Memory bandwidth. The memory efficiency versus the signal pulse length is measured for a storage time of 20 ns with the dressing field. The efficiency is maximal for a 2-ns-long signal. Vertical error bars are the standard deviation of the mean of repeated measurements, and horizontal error bars are 1 standard deviation of the fit uncertainty.

the higher available control power. The efficiency is further improved in FLAME-2 by using a higher OD. In the off-resonance storage, the end-to-end efficiency of FLAME-2 is slightly lower than that of FLAME-1 due to a lower transmission through the vapor cell, caused mainly due to a different signal field detuning, which is on-resonance with the residual ^{85}Rb . The mean number of added noise photons ν in FLAME-2 is lower than in FLAME-1 due to the reduced atomic density in the longer vapor cell and the annular optical pumping beams. Therefore, the noise-to-signal ratio for one input photon, $\mu_1 = \nu/\eta_{e2e}(0)$, is also lower. The lifetime of FLAME-2 is increased by working with a larger signal beam that reduces the time-of-flight broadening and by employing the dressing field to counteract the residual Doppler broadening of the two-photon transition. Overall, FLAME-2 improves on FLAME-1 in all parameters.

The end-to-end memory efficiency, storage time, and acceptance bandwidth are the key ingredients for enhancing photon synchronization rates. In our setup, the memory internal efficiency for on-resonance storage is limited firstly by the finite width of the control beam³⁷, which is only $\sim 60\%$ wider than the signal beam, and by the imperfect optical pumping that causes residual absorption to the $|5P_{3/2}, F=1, 2\rangle$ states. By improving the optical pumping and increasing the control beam waist (while keeping the peak intensity the same), we estimate that an internal efficiency above 70% is readily achievable for on-resonance storage. Further improving the memory internal efficiency will require replacing the Pockels cells that generate the control pulses in order to eliminate the after-pulse and optimize the control shape to the input signal pulse^{35,38}. This can be achieved by using an amplitude electro-optics modulator (EOM) that seeds a tapered amplifier (TA)⁸.

The acceptance bandwidth of the memory is limited by the bandwidth of our control pulses. Using an amplitude EOM to generate the control pulses will thus enable, in principle, the storage of shorter signal photons. However, this will also necessitate higher control powers, which are currently unavailable with tapered amplifiers. Finally, the end-to-end efficiency can be improved by increasing the setup transmission using a vapor cell with higher transmission and an output optical fiber with an anti-reflection coating. Realistically these can increase the overall transmission by about 10%.

In conclusion, we demonstrate an upgraded FLAME with high end-to-end efficiency, high bandwidth, and low noise. It outperforms the original FLAME demonstration in all of these parameters, and we outline a path for further improvements. The upgraded memory can be readily used to synchronize single photons with compatible wavelength and bandwidth, such as those generated in spontaneous cascaded emission^{15,16}.

Methods

Experimental details. The signal field originates from a continuous-wave (CW) distributed Bragg reflector (DBR) laser, which is offset-locked to a stable master laser, and passes through two amplitude EOMs to generate the signal pulses. We use an arbitrary waveform generator (PicoQuant PPG512) to generate Gaussian-like pulses with variable widths and stabilize the bias of the EOMs to achieve a pulse extinction ratio (ER) of $>1:10,000$. We attenuate the signal pulse intensity to an average of ~ 0.1 photons per pulse.

The control field originates from a CW Ti:Sapphire laser. The storage and retrieval control pulses are generated with two free-space Pockels cells between cross-polarizers with a pulse ER of $>1:800$ and peak power at the vapor cell of 1.4 W. The 10–90% rise and fall time of the pulses are ~ 1.2 ns, and the width of the pulses is variable. The timing of the signal and control pulses is controlled by a digital delay generator with a 10 ps timing resolution which operates the experimental sequence at a repetition rate of 10^5 cycles per second.

The auxiliary dressing field originates from an external cavity diode laser. It is initially amplified by an O-Band booster optical amplifier and further amplified by a TA. The dressing power at the vapor cell is set to 135 mW. The pump and repump fields originate from DBR lasers amplified by TAs and have a power of 370 mW (105 mW) for the pump (repump) before the vapor cell. The pump (repump) detuning is -200 MHz ($+150$ MHz). The frequencies of the control and dressing (pump and repump) lasers are stabilized using a wavelength meter with a resolution of 1 MHz (10 MHz).

The signal field is focused to a $1/e^2$ waist radius of $w_0 = 110$ μm inside the vapor cell. The control field has a waist radius of $w_0 = 180$ μm , and the dressing field has a waist radius of $w_0 = 210$ μm . The Rabi frequencies of the control and dressing fields (corresponding to 1.4 W and 135 mW) are $\Omega_c = 640 \pm 50$ MHz and $\Omega_d = 30 \pm 5$ MHz, respectively. The pump and repump annular beam is generated by imprinting an $L = 4$ Laguerre-Gauss phase-mask on the SLM, and has internal (external) diameters of 400 μm (1 mm) inside the vapor cell. This beam is inserted into the vapor cell with a D-shaped mirror at an angle of $\sim 0.85^\circ$ to the optical axis, counter-propagating with respect to the signal field.

Compensating the residual Doppler broadening. For a single excitation, the collective state of the atoms immediately after the first control pulse is^{30,39}

$$|W(0)\rangle = \frac{1}{\sqrt{N}} \sum_j e^{-i\Delta k z_j} |\uparrow\rangle_j \langle \downarrow|_j |G\rangle, \quad (1)$$

where $\Delta k = k_s - k_c$ is the wavevector mismatch of the two-photon transition, z_j is the position of the j th atom, and $|G\rangle = \prod_j |\downarrow\rangle_j$ is the collective ground state. Due to the ballistic thermal motion, after a time t the atoms carry the original phase to position $z_j + v_j t$ and the collective atomic state reads

$$|W(t)\rangle = \frac{1}{\sqrt{N}} \sum_j e^{-i\Delta k(z_j + v_j t)} |\uparrow\rangle_j \langle \downarrow|_j |G\rangle. \quad (2)$$

Neglecting the spontaneous decay of the excited state atoms and the time-of-flight broadening of the atoms moving transversely out of the beam, the storage efficiency versus time is given by $\eta_{\text{int}}(t) = \eta_{\text{int}}(0) \langle |W(0)\langle W(t)| \rangle|^2$ ^{30,39}. Thus, the residual Doppler broadening $\Delta k \neq 0$ induces a decay of the retrieval efficiency.

Adding a far-detuned dressing beam, atom j experiences a light shift of approximately $-\Omega_d^2/(\Delta_d - k_d v_j)$, for $k_d \gg \Delta k$. Expanding to the first order in $k_d v_j/\Delta_d$, the accumulated phase each atom acquires due to the dressing field is

$$\phi_{dj}(t) \approx -\left[\frac{\Omega_d^2}{\Delta_d} + \frac{\Omega_d^2}{\Delta_d^2} k_d v_j \right] t. \quad (3)$$

The first term is a global phase shift, whereas the second term is a velocity-dependent phase shift.

In order to compensate for the residual Doppler broadening, we require that $(\Omega_d^2/\Delta_d^2)k_d v_j + \Delta k v_j = 0$ for all j . This is achieved for the ‘compensation condition’

$$\frac{\Omega_d^2}{\Delta_d^2} \approx \frac{-\Delta k}{k_d}. \quad (4)$$

When this condition is met, to first order in the velocity, the atoms do not experience a velocity-dependent phase. In our experiment, the second-order terms in the velocity and the finite size of the dressing Gaussian beam limit the perfect cancellation of the residual Doppler broadening. In the ladder-level system we employ, $|\Delta k|/k_d \approx 1/110$. This means that at the compensation condition the population in the $28F$ state is negligibly small, and therefore the short-time memory efficiency almost does not deteriorate due to the dressing field.

Data availability

The data that support the findings of this study are available from the corresponding author upon reasonable request.

Received: 27 December 2022; Accepted: 22 May 2023;

Published online: 06 June 2023

References

- O'Brien, J. L. Optical quantum computing. *Science* **318**, 1567–1570 (2007).
- Nunn, J. et al. Enhancing multiphoton rates with quantum memories. *Phys. Rev. Lett.* **110**, 133601 (2013).
- Chanelière, T. et al. Storage and retrieval of single photons transmitted between remote quantum memories. *Nature* **438**, 833–836 (2005).
- Ding, D.-S. et al. Raman quantum memory of photonic polarized entanglement. *Nat. Photonics* **9**, 332–338 (2015).
- Saglamyurek, E., Hrushevskiy, T., Rastogi, A., Heshami, K. & LeBlanc, L. J. Coherent storage and manipulation of broadband photons via dynamically controlled autler–townes splitting. *Nat. Photonics* **12**, 774–782 (2018).
- Novikova, I. et al. Optimal control of light pulse storage and retrieval. *Phys. Rev. Lett.* **98**, 243602 (2007).
- Reim, K. F. et al. Towards high-speed optical quantum memories. *Nat. Photonics* **4**, 218–221 (2010).
- Buser, G., Mottola, R., Cotting, B., Wolters, J. & Treutlein, P. Single-photon storage in a ground-state vapor cell quantum memory. *PRX Quantum* **3**, 020349 (2022).
- Hedges, M. P., Longdell, J. J., Li, Y. & Sellars, M. J. Efficient quantum memory for light. *Nature* **465**, 1052–1056 (2010).
- Lago-Rivera, D., Grandi, S., Rakonjac, J. V., Seri, A. & de Riedmatten, H. Telecom-heralded entanglement between multimode solid-state quantum memories. *Nature* **594**, 37–40 (2021).
- Hain, M., Stabel, M. & Halfmann, T. Few-photon storage on a second timescale by electromagnetically induced transparency in a doped solid. *N. J. Phys.* **24**, 023012 (2022).
- Pittman, T. B., Jacobs, B. C. & Franson, J. D. Single photons on pseudodemand from stored parametric down-conversion. *Phys. Rev. A* **66**, 042303 (2002).
- Kaneda, F., Xu, F., Chapman, J. & Kwiat, P. G. Quantum-memory-assisted multi-photon generation for efficient quantum information processing. *Optica* **4**, 1034–1037 (2017).
- Meyer-Scott, E. et al. Scalable generation of multiphoton entangled states by active feed-forward and multiplexing. *Phys. Rev. Lett.* **129**, 150501 (2022).
- Lee, Y.-S., Lee, S. M., Kim, H. & Moon, H. S. Highly bright photon-pair generation in doppler-broadened ladder-type atomic system. *Opt. Express* **24**, 28083–28091 (2016).
- Davidson, O., Finkelstein, R., Poem, E. & Firstenberg, O. Bright multiplexed source of indistinguishable single photons with tunable ghz-bandwidth at room temperature. *N. J. Phys.* **23**, 073050 (2021).
- Mottola, R. et al. An efficient, tunable, and robust source of narrow-band photon pairs at the 87rb d1 line. *Opt. Express* **28**, 3159–3170 (2020).
- Hsiao, Y.-F. et al. Highly efficient coherent optical memory based on electromagnetically induced transparency. *Phys. Rev. Lett.* **120**, 183602 (2018).
- Wang, Y. et al. Efficient quantum memory for single-photon polarization qubits. *Nat. Photonics* **13**, 346–351 (2019).
- Cao, M., Hoffer, F., Qiu, S., Sheremet, A. S. & Laurat, J. Efficient reversible entanglement transfer between light and quantum memories. *Optica* **7**, 1440–1444 (2020).
- Guo, J. et al. High-performance raman quantum memory with optimal control in room temperature atoms. *Nat. Commun.* **10**, 148 (2019).
- Xu, Z. et al. Long lifetime and high-fidelity quantum memory of photonic polarization qubit by lifting zeeman degeneracy. *Phys. Rev. Lett.* **111**, 240503 (2013).
- Cho, Y.-W. et al. Highly efficient optical quantum memory with long coherence time in cold atoms. *Optica* **3**, 100–107 (2016).
- Wang, Y., Craddock, A. N., Sekelsky, R., Flament, M. & Namazi, M. Field-deployable quantum memory for quantum networking. *Phys. Rev. Appl.* **18**, 044058 (2022).
- Katz, O. & Firstenberg, O. Light storage for one second in room-temperature alkali vapor. *Nat. Commun.* **9**, 2074 (2018).
- Michelberger, P. S. et al. Interfacing ghz-bandwidth heralded single photons with a warm vapour raman memory. *N. J. Phys.* **17**, 043006 (2015).
- Finkelstein, R., Poem, E., Michel, O., Lahad, O. & Firstenberg, O. Fast, noise-free memory for photon synchronization at room temperature. *Sci. Adv.* <http://advances.sciencemag.org/content/4/1/eaap8598> (2018).
- Kaczmarek, K. T. et al. High-speed noise-free optical quantum memory. *Phys. Rev. A* **97**, 042316 (2018).
- Thomas, S. E., Sagona-Stophel, S., Schofield, Z., Walmsley, I. A., & Ledingham, P. M. Single-photon-compatible telecommunications-band quantum memory in a hot atomic gas. *Phys. Rev. Appl.* **19**, L031005 (2023).
- Finkelstein, R. et al. Continuous protection of a collective state from inhomogeneous dephasing. *Phys. Rev. X* **11**, 011008 (2021).
- Fleischhauer, M. & Lukin, M. D. Dark-state polaritons in electromagnetically induced transparency. *Phys. Rev. Lett.* **84**, 5094–5097 (2000).
- Nunn, J. et al. Mapping broadband single-photon wave packets into an atomic memory. *Phys. Rev. A* **75**, 011401 (2007).
- Mu, B.-x. et al. Energy-pooling collisions of rubidium atoms: $\text{Rb}(5P) + \text{Rb}(5P) \rightarrow \text{Rb}(5S) + \text{Rb}(n=5D,7S)$. *Spectrosc. Spectr. Anal.* **26**, 1577 (2006).
- Agrawal, G. *Fiber-Optic Communication Systems* (Wiley, 2021).
- Gorshkov, A. V., André, A., Lukin, M. D. & Sørensen, A. S. Photon storage in A-type optically dense atomic media. ii. free-space model. *Phys. Rev. A* **76**, 033805 (2007).
- Biraben, F., Bassini, M. & Cagnac, B. Line-shapes in doppler-free two-photon spectroscopy. the effect of finite transit time. *J. Phys. Fr.* **40**, 445–455 (1979).
- Surmacz, K. et al. Efficient spatially resolved multimode quantum memory. *Phys. Rev. A* **78**, 033806 (2008).
- Gorshkov, A. V., André, A., Fleischhauer, M., Sørensen, A. S. & Lukin, M. D. Universal approach to optimal photon storage in atomic media. *Phys. Rev. Lett.* **98**, 123601 (2007).
- Whiting, D. J., Šibalić, N., Keaveney, J., Adams, C. S. & Hughes, I. G. Single-photon interference due to motion in an atomic collective excitation. *Phys. Rev. Lett.* **118**, 253601 (2017).

Acknowledgements

We thank Ran Finkelstein for helpful discussions. We acknowledge financial support from the Israel Science Foundation, the US-Israel Binational Science Foundation (BSF) and US National Science Foundation (NSF), the Minerva Foundation with funding from the Federal German Ministry for Education and Research, the Estate of Louise Yagour, and the Laboratory in Memory of Leon and Blacky Broder.

Author contributions

O.D., E.P., and O.Y. designed and built the experiment. O.D. and O.Y. performed the experiment and the data analysis. E.P. and O.F. supervised the project. All authors discussed the results and contributed to writing the manuscript.

Competing interests

The authors declare no competing interests.

Additional information

Correspondence and requests for materials should be addressed to Omri Davidson.

Peer review information *Communications Physics* thanks the anonymous reviewers for their contribution to the peer review of this work.

Reprints and permission information is available at <http://www.nature.com/reprints>

Publisher's note Springer Nature remains neutral with regard to jurisdictional claims in published maps and institutional affiliations.



Open Access This article is licensed under a Creative Commons Attribution 4.0 International License, which permits use, sharing, adaptation, distribution and reproduction in any medium or format, as long as you give appropriate credit to the original author(s) and the source, provide a link to the Creative Commons license, and indicate if changes were made. The images or other third party material in this article are included in the article's Creative Commons license, unless indicated otherwise in a credit line to the material. If material is not included in the article's Creative Commons license and your intended use is not permitted by statutory regulation or exceeds the permitted use, you will need to obtain permission directly from the copyright holder. To view a copy of this license, visit <http://creativecommons.org/licenses/by/4.0/>.

© The Author(s) 2023